Light-force-induced shift in laser spectroscopy of atomic helium

X. Zheng (郑昕),[1,2,*] Y. R. Sun (孙羽),[1,2,†] J.-J. Chen (陈娇娇),[1] J.-L. Wen (温金录),[1] and S.-M. Hu (胡水明)[1,2]

[1]*Hefei National Laboratory for Physical Sciences at Microscale, iChem Center, University of Science and Technology of China, Hefei 230026, China*

[2]*CAS Center for Excellence in Quantum Information and Quantum Physics, University of Science and Technology of China, Hefei 230026, China*

(Received 30 November 2018; published 12 March 2019)

A laser-power-dependent shift has been observed in various atomic beam spectroscopy measurements, which was often treated by extrapolating the results to the zero-field limit. Here we present an experimental and theoretical study of this effect in the measurements of the $2\,^3S$-$2\,^3P$ transition frequency of ^{4}He. The light-force-induced shift was attributed as a result of modulated atomic trajectories induced by the standing-wave laser field and consequent distortions in the lineshape. Modulation of the beam spatial distributions was detected by imaging atoms at high laser power and was also simulated by the Monte Carlo wave-function approach. The nonlinear behavior of the light-force-shift was observed experimentally and reproduced by the simulations. The systematic shift in the extrapolated result at the zero-field limit was analyzed. As a consequence of this effect, a correction of +0.50(80) kHz was added to our previous result on the $2\,^3S_1$-$2\,^3P_1$ transition frequency [Phys. Rev. Lett. **119**, 263002 (2017)], and the reevaluated value is 276 734 477 704.3(1.6) kHz.

DOI: 10.1103/PhysRevA.99.032506

I. INTRODUCTION

Precision spectroscopy in few-electron atomic systems, such as hydrogen and helium, is an ideal tool for tests of the quantum-electrodynamics (QED) theory and determination of the fundamental physical constants, such as the Rydberg constant R_∞ and the fine-structure constant α [1–6]. However, there are still significant discrepancies among some latest experimental and theoretical results, including that in the spectroscopy of atomic hydrogen which leads to the so-called "proton-size puzzle" [7], indicating that more investigations into the experiments and calculations are needed.

Laser spectroscopy of atoms in a collimated beam has been used in various studies to determine the transition frequencies. For example, the frequency of the $2S$-$4P$ transition of H was determined with an uncertainty of 2.3 kHz, which is 0.017% of the natural linewidth [8]. The $2\,^3S$-$2\,^3P$ transition of He was measured to 1–2 kHz precision [9,10], which is 0.1% of the natural linewidth of the transition. In these measurements, counterpropagating laser beams were used to eliminate the first-order Doppler shift, which formed a coherent standing-wave laser field when their wavefronts were properly retraced [11]. It has been commonly assumed that the spectroscopy lineshape should be symmetric around its resonance center if the laser intensity is sufficiently low.

However, asymmetry has been found in fluorescence spectroscopy by using strongly interacting standing-wave lasers [12,13] and Lamb-dip spectroscopy [14,15]. Substantial asymmetry contributes to systematic shifts in the observed resonances. A classical treatment taking into account the mechanical effect of the standing-wave field can be achieved by solving the optical Bloch equations by using a position-dependent Rabi frequency simultaneously with Newton's equation of motion [16,17]. But the attempt to correct for this shift using numerical calculations relies on the theoretical model and accuracy of input parameters such as the atomic velocity distribution, laser geometry, and intensity. An alternative approach is to extrapolate the observed shift as a linear function of the laser power to the zero-field limit [6,18,19]. Since moderate laser powers are needed to maintain a sufficient signal in most spectroscopy measurements, it remains questionable about the validity of the linear extrapolation, which may lead to possible offset from the "true" resonance center.

In this paper, we present an experimental and theoretical study of the light-force-induced shift. Spectroscopy of the $2\,^3S$-$2\,^3P$ transition in atomic ^{4}He was used as a prototype to investigate this effect. A nonlinear behavior of the light-force shift against the laser power was observed. Simulations of the light-force effect were also carried out by using the Monte Carlo wave-function (MCWF) approach [20,21], which reproduces well the nonlinear behavior. Analysis of the experimental and simulation results allows us to reevaluate the uncertainty due to the light-force-induced shift in our previous spectroscopy measurements.

II. EXPERIMENTS

The experimental configuration for the $2\,^3S$-$2\,^3P$ spectroscopy of ^{4}He is shown in Fig. 1(a), which is similar to the one presented in our previous studies and will be only briefly described here. Helium atoms were prepared in the $2\,^3S_1$ metastable state via radio-frequency discharge, and were subsequently collimated and deflected by two-dimensional

*Present address: Department of Physics, University of Wisconsin-Madison, 1150 University Avenue, Madison, Wisconsin 53706, USA.

†Corresponding author: robert@ustc.edu.cn

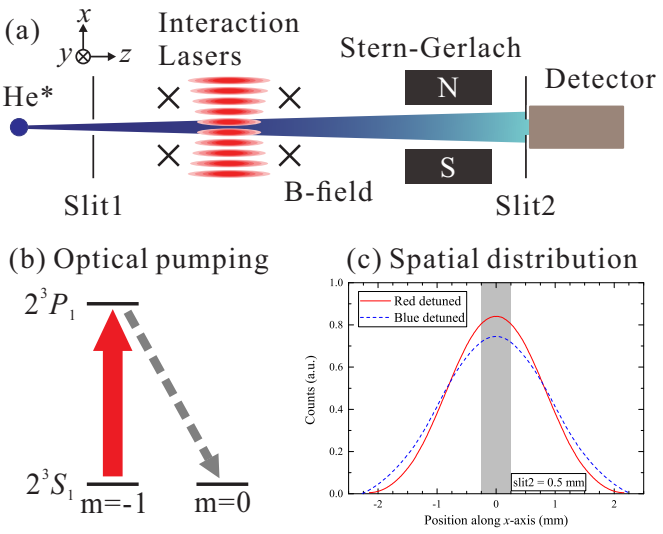

FIG. 1. (a) Illustration of experimental setup (not to scale). (b) Optical pumping by the probe laser. (c) Simulated atomic beam spatial distributions induced by red (solid line) and blue (dashed line) detuned standing-wave laser field, respectively. The shaded area represents slit2.

transverse cooling. Two slits with a width of 0.5 mm were placed 1.5 m apart in the beam. The first one (slit1) was placed after the deflection region, and the second one (slit2) was placed before the detector, which consists of a three-layer microchannel plate, a phosphor screen, and an electron-multiplying charge-coupled device (CCD). A Stern–Gerlach magnet was used to deflect atoms at the $m = \pm 1$ levels to ensure that only atoms at the $m = 0$ level pass through slit2 and reach the detector.

Before entering the spectroscopy region, the atoms in the $2\,^3S_1$ ($m = 0$) state were optically pumped to either the $m = \pm 1$ states, depending on the polarization of the pump laser beam ($\sigma^{\pm}$). The $2\,^3S_1$ ($m = 0$) state was repopulated [Fig. 1(b)] when the atoms interacted with the probe laser which scanned through resonance of the $2\,^3S_1$-$2\,^3P_J$ transition ($J = 1$ in this paper, for instance). This spectroscopy region was shielded with three layers of cylindrically shaped μ metal. A homogeneous magnetic field, which defined the quantization axis along gravity, was generated by a cosine theta coil inside the magnetic shield.

The probe laser was a home-built external cavity diode laser, phase locked to a narrow-linewidth fiber laser which was frequency stabilized to a Fabry-Pérot cavity made of ultralow-expansion glass. The probe laser beam was coupled into a polarization-maintaining single-mode fiber, and its intensity was stabilized by using a noise eater. To eliminate the first-order Doppler shift, the probe laser beam was retroreflected to form a standing-wave laser field.

Modulation of atomic trajectories induced by standing-wave laser field

Besides the optical pumping effect depicted in Fig. 1(b), the standing-wave laser field also introduces mechanical effects on the atoms. The laser field modulates the atomic beam trajectories oppositely at different detunings around the resonance center. When red detuned, the atomic beam is transversely cooled and thus gets focused. In case of blue detuning, the atomic beam is diverged due to the transverse heating effect. Figure 1(c) shows the simulated spatial distributions of the atomic beam, assuming a Gaussian profile for the initial distribution. Since the slit before the detector (slit2) is relatively narrow, changes in the spatial distributions would lead to substantial differences in counting rates: the count increases in the red wing and decreases in the blue wing. As a result, this effect introduces asymmetry in the spectral line profile.

To observe the spatial modulation effect by the standing-wave laser field, we replaced the 0.5 mm slit2 with a broader 2-mm-wide slit. Images of the spatial distributions of the metastable helium atoms were taken at different laser frequencies. The laser intensity (one-way) was set to be $2I_{\rm sat}$ in order to saturate this transition. The experimental procedure for differential images was as follows: We took images using a CCD camera by switching the laser frequency with red detuned ($\mathrm{P_{red}}$), blue detuned ($\mathrm{P_{blue}}$), and on resonance ($\mathrm{P_{ref}}$), respectively. The images taken on resonance were used as a reference, such that we obtained differential images, $\delta\mathrm{P_{red}} = \mathrm{P_{red}} - \mathrm{P_{ref}}$, and $\delta\mathrm{P_{blue}} = \mathrm{P_{blue}} - \mathrm{P_{ref}}$. Each image was an average of 100 shots. A clear contrast can be seen in Fig. 2, indicating that the atoms got focused in the case of red detuning, but got diverged for blue detuning. The results agree well with the simulation shown in Fig. 1(c). In the spectroscopy measurement, a narrow slit is necessary to reduce the first-order Doppler broadening, and the "count" on the detector is a combination of atoms that both pass through the slit and reach the detector. The spatial modulation shown in Fig. 2 would result in systematic distortions on the spectral line profile, and the fitted line center would be redshifted from the resonance center due to this distortion. Because it originates from the mechanical effects of the laser field, this systematic shift also manifests a laser-power-dependent feature.

For heavy atoms such as cesium, a similar effect was only observed in an intense laser field [13], because the atom recoil was sufficiently small. Under the experimental conditions of helium or hydrogen, the saturation factor was chosen to be considerably smaller. For example, in case of helium spectroscopy, the laser intensity applied in the $2\,^3S_1(m = -1) \rightarrow 2\,^3P_1(m = -1)$ spectroscopy measurement was restricted to $I/I_{\rm sat} \leqslant 0.3$. Each atom scattered no more than five photons before it was optically pumped to the "dark" state $2\,^3S_1(m = 0)$. Such a light force was thought to be considerably small. However, because of the light mass of helium, the recoil velocity when the atom absorbs or emits a photon is $v_{\rm rec} = \hbar k/m = 0.091\,\mathrm{m/s}$, which is a factor of 23% compared with the Doppler velocity $v_{\rm Dop} = \sqrt{\hbar\Gamma/m} = 0.40\,\mathrm{m/s}$. Therefore, the light force is no longer negligible, and this effect will be analyzed in the next section.

III. THEORETICAL APPROACH

To simulate atomic trajectories modulated by the standing-wave laser field, we follow the Monte Carlo wave-function approach developed by Dalibard *et al.* [20,21]. We start from a master equation describing the dynamics of open quantum systems, and the Monte Carlo method is used to simplify the

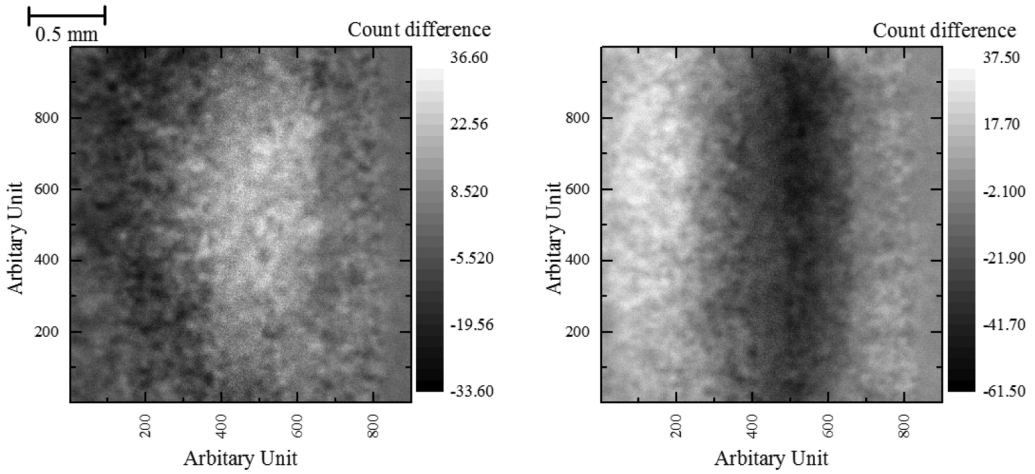

FIG. 2. Differential images taken at red (left, δP_{red}) and blue (right, δP_{blue}) detunings, respectively, by using image taken at resonance as a reference. Each image was averaged by 100 shots recorded by a CCD camera. The horizontal and vertical axes correspond to the x axis and y axis, respectively.

calculations. Descriptions of the master equation is given in the Appendix.

A. Model of simulation

We consider a three-level atomic system, which consists of an excited state $|e\rangle$, a ground state $|g\rangle$, and a dark state $|0\rangle$. The atoms are originally populated at $|g\rangle$, and only those populated at $|0\rangle$ contribute to the detected signal. The direction of the atomic beam is denoted as the z axis, while the probe laser propagates along the x axis (see Fig. 1). Note that the magnetic field is along the y axis, perpendicular to the wave vector. For simplicity, the atoms have a uniform longitudinal velocity of v_{mean} along the z axis. For the transverse velocity, we consider only the degree of freedom along the x axis, with an initial transverse velocity of v_{x00}. The $\{|e, p\rangle, |g, p\rangle\}$ basis is used. The momentum space is discretized with a step size of $\hbar k$, where $k = 2\pi/\lambda$ is the wave vector of the probe laser, according to the quantum nature of absorbed or emitted photon momentum. Therefore, the wave function reads

$$\begin{aligned}|\Psi(t)\rangle &= |e/g\rangle \otimes |p = \pm n\hbar k\rangle \\ &= \alpha_n(t)|e, n\hbar k\rangle + \beta_n(t)|g, n\hbar k\rangle, \end{aligned} \tag{1}$$

where coefficients $\alpha_n(t)$ and $\beta_n(t)$ correspond to components of the excited and ground states with momentum $n\hbar k$ along x at time t, respectively. We choose $n_{\max} = 10$, which gives sufficient description for the atomic trajectories without too much computational cost.

The system Hamiltonian H_S in the interaction picture reads

$$H_S = P^2/2m + \hbar\Omega\cos(kX)(S^+ + S^-) - \hbar\Delta P_e, \tag{2}$$

where X and P are the atomic position and momentum operators, $P_e = |e\rangle\langle e|$ is the projection operator onto state $|e\rangle$, $\Delta = \omega - \omega_0$ is the laser detuning, and Ω is the Rabi frequency of each traveling wave forming the standing wave. Under the evolution of the effective Hamiltonian, $H_{\text{eff}} = H_S - (i\hbar\Gamma/2)P_e$, the coefficients $\alpha_n(t)$ and $\beta_n(t)$ are governed by

$$\begin{aligned}\alpha_n(t) \to \alpha_n(t+\delta t) &= \left(1 - i\frac{\delta t}{\hbar}\frac{(n\hbar k)^2}{2m} + i\Delta\delta t - \frac{\Gamma}{2}\delta t\right)\alpha_n(t) \\ &\quad - \frac{i\delta t\Omega}{2}[\beta_{n+1}(t) + \beta_{n-1}(t)], \\ \beta_n(t) \to \beta_n(t+\delta t) &= \left(1 - i\frac{\delta t}{\hbar}\frac{(n\hbar k)^2}{2m}\beta_n(t)\right) \\ &\quad - \frac{i\delta t\Omega}{2}[\alpha_{n+1}(t) + \alpha_{n-1}(t)]. \end{aligned} \tag{3}$$

As is seen in Eq. (3), the laser field couples the state $|g\rangle$ and $|e\rangle$, along with momentum exchange by ± 1 in the subscripts of coefficients α and β. This corresponds to the photon recoils during absorption and stimulated emissions.

As for the spontaneous emissions including recoils, we choose a coarse discretization for the emitted photon, with a step size of $\hbar k'$, i.e., $k' = -k$, 0, or k. Depending on the momentum and polarization, the "quantum jump" operators in Eq. (A6) can be simplified as

$$C_q(k') = \sqrt{\Gamma\bar{p}_q(k')}e^{-ik'X}(\epsilon_q^* \cdot S^-), \tag{4}$$

where $\epsilon_0 = e_z$ corresponds to π polarization, and $\epsilon_\pm = \mp\frac{1}{\sqrt{2}}(e_x \pm ie_y)$ corresponds to $\sigma^\pm$ polarization. The probability $\bar{p}_q(k')$ for the nine jump operators can be calculated by integrating over the angular patterns of light emitted by an oscillating dipole.

B. Monte Carlo wave-function approach

Here we discuss treatment of evolutions in the laser field. Instead of solving the density matrix, we apply an alternative approach based on Monte Carlo evolution of wave functions. This approach benefits by less computational cost, since a wave function ($\propto N_{\text{states}} = 42$) is a smaller object compared with a density matrix ($\propto N_{\text{states}}^2 \approx 1600$). The MCWF approach is rather straightforward following recipes developed by Dalibard *et al.* [20,21].

Consider at time t the *system* with a normalized wave function $|\Psi(t)\rangle$. After a time step δt, which must be chosen small enough to ensure the validity of the calculations at first order [20,21], the wave function at time $t+\delta t$ is obtained by action of the effective Hamiltonian H_{eff}:

$$H_{\text{eff}} = H_S - \frac{i\hbar}{2}\sum_m C_m^\dagger C_m, \tag{5}$$

where C_m are the quantum jump operators.

This yields for sufficiently small δt, the wave function at time $t+\delta t$ evolves as

$$|\Psi^{(1)}(t+\delta t)\rangle = \left(1 - \frac{iH_{\text{eff}}\delta t}{\hbar}\right)|\Psi(t)\rangle. \tag{6}$$

It can be seen that the new wave function is not normalized, since H_{eff} is non-Hermitian. Hence, through normalization, the square of its norm yields

$$\langle\Psi^{(1)}(t+\delta t)|\Psi^{(1)}(t+\delta t)\rangle = 1 - \delta p + O(\delta t^2). \tag{7}$$

In this expression, we have introduced the probability δp, which is defined as

$$\delta p = \delta t \frac{i}{\hbar}\langle\Psi(t)|H - H^\dagger|\Psi(t)\rangle = \sum_m \delta p_m,$$
$$\delta p_m = \delta t\,\langle\Psi(t)|C_m^\dagger C_m|\Psi(t)\rangle \geqslant 0. \tag{8}$$

Another possibility for evolving the wave function is to apply the quantum jump operators C_m, which describe possible "directions" for decay in different channels. The quantum jump evolution can be achieved by applying one of those operators to the wave function at time t.

Using Eq. (8), we find that the total probability for making a jump is δp. The no-jump case occurs with probability $1-\delta p$. The random choice between the two evolutions is performed by picking a pseudorandom number ϵ_p uniformly distributed in [0,1], which is then compared with δp.

If $\epsilon_p > \delta p$, we simply normalize the wave function $|\Psi^{(1)}(t+\delta t)\rangle$:

$$|\Psi(t+\delta t)\rangle = \frac{|\Psi^{(1)}(t+\delta t)\rangle}{\|\Psi^{(1)}(t+\delta t)\rangle\|}. \tag{9}$$

Otherwise, if $\epsilon_p < \delta p$, then, among m possible quantum jumps, a second random choice determines which jump occurs, according to the probability law $\Pi_m = \delta p_m/\delta p$. The wave function after the quantum jump at time $t+\delta t$ is given by:

$$|\Psi(t+\delta t)\rangle = \frac{C_m|\Psi(t)\rangle}{\|C_m|\Psi(t)\rangle\|}. \tag{10}$$

The quantum jump operators, corresponding to spontaneous emissions in our case, can be divided into two decay paths: (1) from $|e\rangle$ to $|g\rangle$, where another non-Hermitian evolution starts; and (2) from $|e\rangle$ to $|0\rangle$, the atom enters the dark state and runs out of interactions. The possibilities for decaying into one of the two paths are determined by their branching ratios.

C. Input parameters and simulation procedure

The atoms are assumed to be initially populated in the ground state, and in a superposition of different transverse momentum eigenstates. The initial transverse momentum populations are assumed to be in a Gaussian distribution $e^{-v_x^2/2\sigma_x^2}$, where σ_x is determined by the Doppler velocity $v_{\text{Dop}} = 0.40$ m/s. The atoms start at slit1, with a width of 0.5 mm and a position step size of 0.005 mm. All the atoms are considered to have a uniform longitudinal velocity of $v_{\text{mean}} = 700$ m/s, since we observed a relatively small distribution of 50 m/s (full width at half maximum, FWHM) [9]. Power loss in the retroreflected laser beam was considered by introducing a factor of $\delta I = 5\%$.

The evolution of atomic trajectories consists of three steps: (1) Atoms propagate freely from slit1 to the spectroscopy region at a distance l_1. (2) Atoms interact with the standing-wave laser field, with an total interaction time of $2w_0/v_{\text{mean}} \approx 4.5\ \mu$s, where w_0 is the $1/e^2$ beam waist. In this step, the MCWF method described in Sec. III B is applied to derive the momentum distributions after interaction. (3) Atoms propagate freely again, carrying a modified momentum distribution, from the spectroscopy region to slit2 with a distance of l_2. For detection, we count atoms at the dark state $|0\rangle$ and within the range of 0.5-mm-wide slit2. This implies that both internal state selection and spatial selection effects contribute to the spectroscopic signal. At a given laser intensity of I, we scanned the laser frequency with a detuning Δ varying from $-2.5\,\Gamma$ to $+2.5\,\Gamma$, where $\Gamma = 2\pi \times 1.62$ MHz is the natural linewidth of the transition. Different step sizes ranged from 0.1 to 0.5 Γ were adopted. The simulated spectra were fit with a Lorentzian profile to derive the resonance center.

Because of the stochastic nature of Monte Carlo procedure, one has to average numerous results in order to reduce the statistical uncertainty. Depending on the targeted precision, the number of averaging n_{avg} for one spectra was chosen to be from 10^3 to 10^5. As a result, typical uncertainty in the line center from one spectra is about 2–6 kHz at low laser intensities. At high laser intensities, fewer averaging numbers were used since the light-force-induced lineshape distortion becomes more substantial. The evolution time step δt is set to be 2 ns, which corresponds to $1/50\ \Gamma^{-1}$, as a compromise between the computational cost and the accuracy. We also tried to run part of the simulations with a much smaller step size of $\delta t = 1/1000\ \Gamma^{-1} = 0.1$ ns, but found no deviations under 2 kHz statistical uncertainty for a single spectra. The parameters we used in our Monte Carlo simulations are summarized in Table I.

IV. SIMULATION RESULTS COMPARED TO MEASUREMENTS

In this section, we present the numerical results of our Monte Carlo simulation. Our simulated spectra reproduces the characteristics observed in experimental spectra. By tuning the saturation factor of the laser field, the nonlinear behavior of the power-dependent shift is also obtained, which agrees well with our experimental results. At low laser intensities, the simulation gives a reasonably good linear dependence on the laser intensity. To evaluate our standard extrapolation

TABLE I. Monte Carlo simulation parameters.

Name	Symbol	Value
Number of simulations	$N_{\rm sim}$	3×10^7
Atom mass	m	4 a.u.
Natural linewidth	Γ	$2\pi \times 1.62$ MHz
Excited state lifetime	τ	98 ns
Wavelength	λ	1083.3 nm
Recoil velocity	$\hbar k/m$	0.091 m/s
Saturation intensity	$I_{\rm sat}$	167 μW/cm^2
Saturation factor	$I/I_{\rm sat}$	0.04-4
Number of momentum eigenstates	$2n_{\rm max}+1$	21
Distance from slit1 to probe	l_1	55 cm
Distance from probe to slit2	l_2	105 cm
Initial slit width	x_1	0.5 mm
Initial position step	δx_1	0.005 mm
Detection slit width	x_2	0.5 mm
Initial transverse velocity spread	σ_x	0.40 m/s
Laser beam waist	w_0	1.6 mm
Mean longitudinal atom velocity	$v_{\rm mean}$	700 m/s
Interacting time	t	4.5 μs
Interacting time step	δt	2 ns
Retro-reflected beam power loss	δI	5%

approach to determine the "zero-field" value of the resonance center, the line centers derived from the simulated spectra were extrapolated to the zero-field limit and the offset from the resonance center was obtained.

A. Comparison of simulated and experimental spectra

By using the tool of MCWF and defined parameters as input, we obtained the light-force-induced shift at different laser intensities. As the laser power increases, the probability of a quantum jump into the dark state $|0\rangle$ also increases, which subsequently reduces computational efforts. Since power broadening dominates at high laser intensities, an accuracy of a few tens of kHz is sufficient for the simulation.

Figure 3(b) shows a spectra simulated under laser intensity of $I = 2.3\,I_{\rm sat}$, initial transverse velocity spread $\sigma_x = 0.40$ m/s, and an averaging number $n_{\rm avg}$ of 200. It reproduces well the experimental spectra given in Fig. 3(a). The characteristics in both spectra are shown clearly: counts on the red side near the line center are enhanced, while they decrease on the blue side. If we fit the spectrum with a simple Lorentzian profile, the "center" derived from the fit is redshifted. The shifts obtained from spectra simulated at different laser intensities are shown in Fig. 4. The observed redshifts are increased as the saturation factor is tuned from 0.4 to 4, and also manifests a nonlinear dependence at high laser intensities. A comparison with the experimental data under similar laser intensities is also shown in Fig. 4, indicating a good agreement between the simulations and experimental results. It also demonstrates the validity of the MCWF approach.

B. Extrapolation to the zero-field limit

At low laser intensities, the saturation factor is smaller, ranging from 0.04 to 0.3 in our simulations, and the lineshape distortion becomes less significant. As a result, the possibility

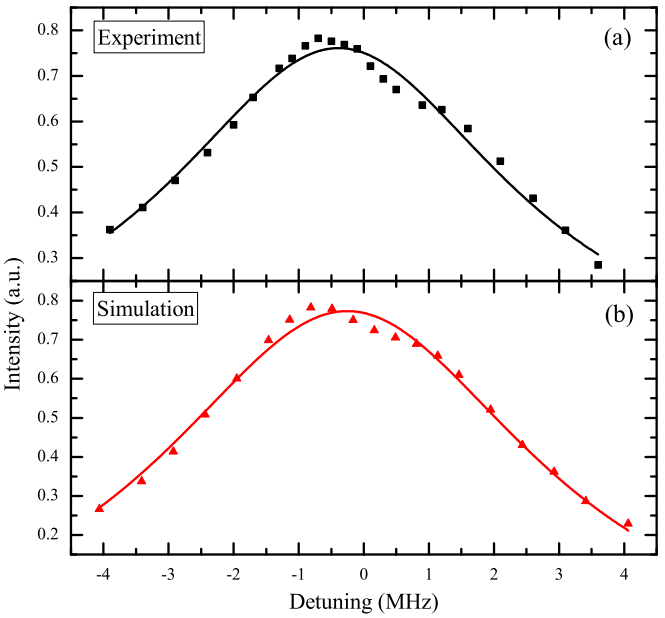

FIG. 3. (a) Illustration of lineshape distortion observed in experiment (square), with a probe intensity of $2.3I_{\rm sat}$. The distortion is substantial in the high-intensity regime. (b) Simulated spectrum (triangle) using Monte Carlo wave-function approach, which reproduces the observed distortion. The solid lines represent spectra fitted using Lorentzian profiles.

of a quantum jump decreases significantly. However, because we are looking for a substantial light-force-induced shift on the sub-kHz level, a much larger averaging number and more computational efforts are required in the simulations.

Four different laser intensities, $I/I_{\rm sat} = 0.04$, 0.07, 0.14, and 0.28, were adopted here. Typical statistical accuracy of the simulation at each intensity was about 1 kHz, with an average number $n_{\rm avg}$ of more than 10^5. The spectra were fit with Lorentzian functions and the light-force-induced shift derived from the fit is shown in Fig. 5, and is consistent with our experimental data.

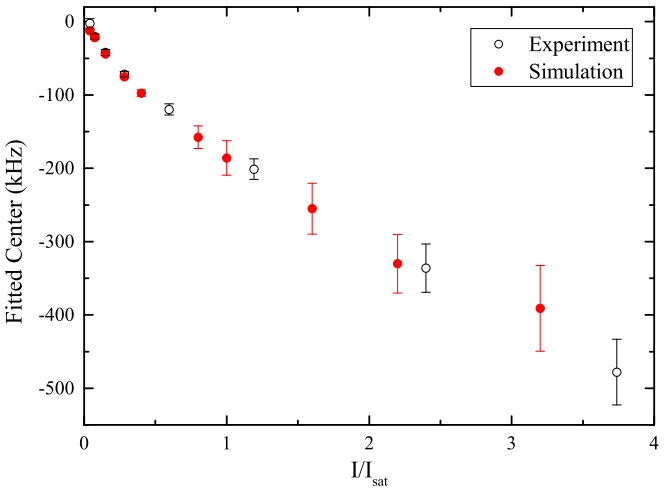

FIG. 4. Comparison of the laser-force-induced shifts obtained from the experiment (open circles) and from the simulation (filled circles). The laser intensity given here stands for the injected beam intensity for probe laser (one way).

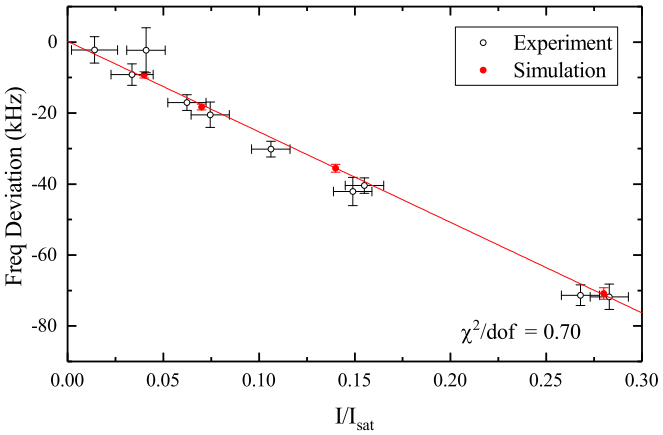

FIG. 5. Comparison of experimental (open circles) and simulated (filled circles) light-force-induced shifts obtained at low laser intensities. One group set of simulated data is shown. The laser intensity given here stands for the injected beam intensity for the probe laser (one way). The solid line represents a linear fit of simulation, with a fitting function $y = 0.22(85) - 255(7)x$, and a reduced chi-squared of 0.70.

Instead of using our numerical calculations to correct for this shift, we apply a linear extrapolation of the shifts (line "centers") to the zero-laser-power limit. This method was more frequently used in various studies, since it works without accurate knowledge of experimental parameters such as the laser beam geometry and absolute laser intensities. However, this approach relies on the assumption that the observed shift has a linear dependence on the laser intensity. As we have shown in Fig. 4, it fails at high laser intensities. To reduce this nonlinear effect, we set a maximum intensity of $I/I_{\text{sat}} = 0.30$ used in the extrapolation, therefore minimizing the nonlinear effect while preserving the spectroscopic signal-to-noise ratio.

However, the nonlinear behavior of the power-dependent shift might contribute to possible frequency offset in linear fittings, even though we worked in the low-intensity regime. To quantitatively assess this systematic shift, we ran six independent groups of simulations, with a total number of more than 5×10^6 MCWF simulations, and extrapolated the

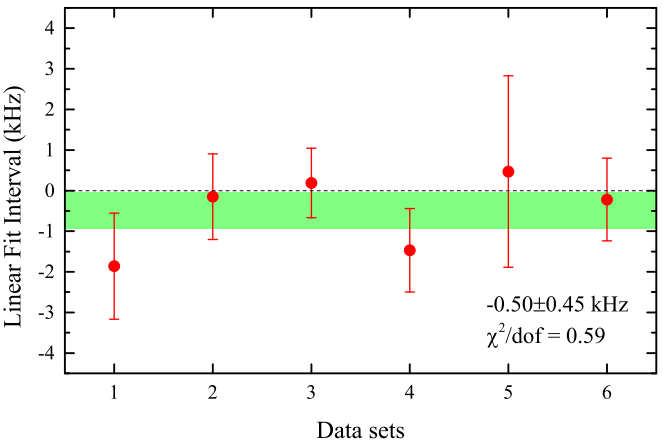

FIG. 6. Weighted statistics of the linear fit intervals in simulations. The shaded region represents 1σ standard deviation.

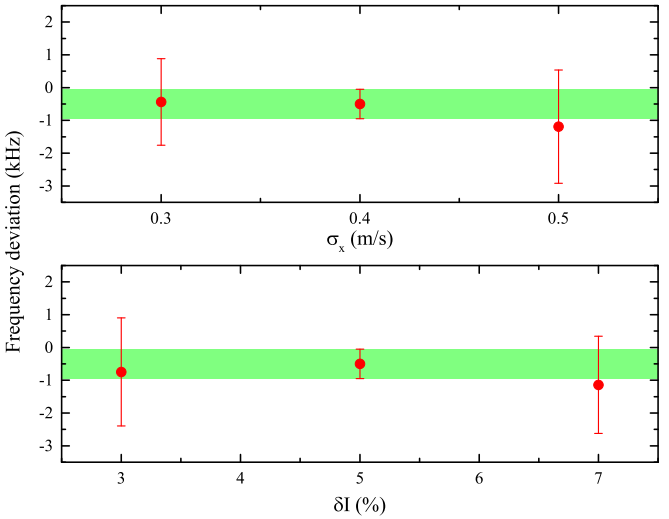

FIG. 7. Simulation results by varying the Monte Carlo input parameters, the initial transverse velocity distribution σ_x and retroreflection beam loss δI.

frequency shifts obtained at different laser intensities to obtain the zero-field limit. The solid line shown in Fig. 5 presents an example of the extrapolation. The reduced chi-square for a single linear fit ranged from 0.3 to 2. For each group of simulations, the linear fit interval, the offset from the "true" resonance center, was obtained. For linear fits with reduced chi-squared larger than unity ($\chi^2/\text{dof} > 1$), the error bar of the result was inflated by a factor of $\sqrt{\chi^2/\text{dof}}$. Statistics of the results obtained from these six groups of simulations is shown in Fig. 6. The weight-averaged shifts at $I/I_{\text{sat}} = 0$ was determined to be -0.50 ± 0.45 kHz with a reduced chi-squared of 0.59 (see Fig. 6).

Our simulations show that by extrapolating results obtained below $I/I_{\text{sat}} = 0.3$ to the zero field, the residual light-force-induced shift is around -0.5 kHz, with an uncertainty of also about 0.5 kHz mainly from statistics. We also carried out simulations with different input parameters, such as the initial transverse velocity spread σ_x and retroreflected beam power loss δI. Using a σ_x of 0.4 ± 0.1 m/s and a δI of $5\% \pm 2\%$, we found the derived fit intervals consistent with each other within current statistical uncertainty. The simulated results for various input parameters are shown in Fig. 7.

C. Methods to suppress light-force-induced effect

As discussed above, the light-force-induced shift actually comes from the modification of the spatial distributions of the atoms and eventually changes the ratio passing through the second slit. Since a wider slit would be less sensitive to the spatial distribution of the atoms, we can in principle reduce this effect by using a wider slit. Simulations under different slit widths were carried out and the results are shown in Fig. 8. It turns out that the light-force shift can be suppressed by a factor of three, as the slit width x_2 varies from 0.5 to 2 mm. This effect can be dramatically suppressed by an order of magnitude by replacing slit2 with a slit of 5 mm width. In practical experiments, however, it comes with the price of larger Doppler broadening and increasing

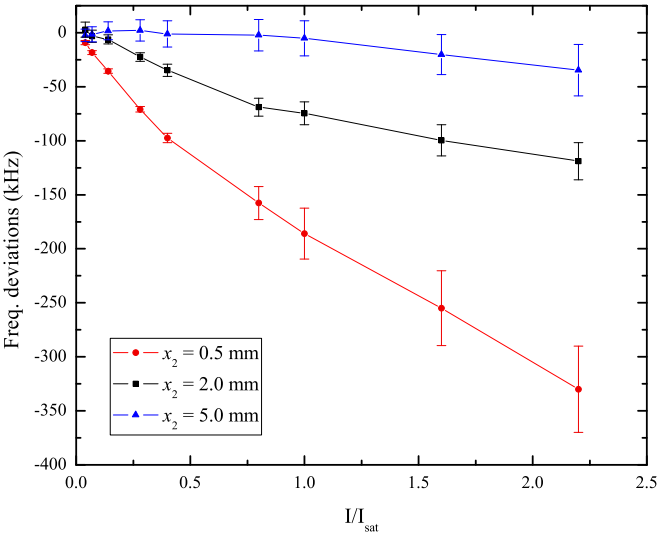

FIG. 8. Demonstration of suppressing light-force-shift by simulations using different x_2 of 0.5 mm (circles), 2.0 mm (squares), and 5.0 mm (triangles). The horizontal axis stands for single-beam intensity for probe laser.

background noise since the detector receives more hot atoms and scattering lights when a wider slit is used. Moreover, the size of the detector also limits the effective width of the slit.

As an alternative method to reduce the light-force effect due to the standing-wave field, instead of using a retroreflecting probe laser, one can rapidly switch between two counterpropagating traveling-wave laser beams. Since each time the atoms interact with only one laser beam, the optical molasses effect would be eliminated. Therefore, the light-force shift can be considerably suppressed while preserving cancellation of the first-order Doppler shift. In that case, a new challenge arises for a dedicated control of the wavefronts of the laser beams, since imperfect overlap of the wavefronts might result in residual first-order Doppler shift. Possible systematic effects from the phase difference between the two lasers should be considered.

A more appropriate method would be to run the experiments under ultralow laser power (<100 nW, $I/I_{\rm sat} < 0.01$), which would reduce the light-force shift by another order of magnitude. This method comes with the price of sacrificing the signal-to-noise ratio, since the excitation rate is proportional to the laser power. This problem might be overcome with our next generation atomic beam setup, which has a metastable atomic helium beam flux at the level of 10^{11} atoms/(sr s), two orders of magnitude larger than that used in our previous studies. Therefore, we expect to preserve the spectroscopic signal-to-noise ratio while reducing the light-force induced shift by an order of magnitude.

D. Consequences on previous measurements of $2\,^3S$-$2\,^3P$ transitions of ^{4}He

Here we discuss the consequence of the light-force-induced shift on our previous measurements of the $2\,^3S$-$2\,^3P$ transitions of ^{4}He [6,9,19]. In the $2\,^3S_1$-$2\,^3P_1$ measurement [9], the typical uncertainty for one-day-averaged data ranged from 2 to 5 kHz. Under such precision, we were unable to find significant nonlinear behavior between the line center and the laser power. However, according to our simulations, along with the power-dependent shift and the nonlinear behavior in case of high laser powers, we realized that the uncertainty for the light-force effect was underestimated. Note that the maximum laser intensity we used in the extrapolation was about $0.25I_{\rm sat}$, being close to that used in the simulations given above. Taking into account the results shown in Fig. 6 and variations from different input parameters (σ_x and δI), we conservatively assigned a systematic correction of $+0.50(80)$ kHz for the light-force-induced effect. Therefore, the reevaluated $2\,^3S_1$-$2\,^3P_1$ transition frequency was 276 734 477 704.3(1.6) kHz.

We are aware of a recent microwave study on the $2\,^3P_1$-$2\,^3P_2$ fine-structure interval by Kato *et al.* [22], which differs from our previous results [6,19] by about -1 kHz (4.9σ). Here we discuss possible contributions from the light-force effect in this discrepancy. Because the light-force effect largely cancels in the frequency difference of two optical transitions, the observed power dependence for the $2\,^3P_1$-$2\,^3P_2$ interval is about -0.8 kHz/μW [19], which is only 1/20 of the power dependence for the $2\,^3S_1$-$2\,^3P_1$ transition. Since the correction due to the light-force effect was $+0.50(80)$ kHz for $2\,^3S_1$-$2\,^3P_1$ transition, we estimate that it should be no more than $+25(40)$ Hz for the $2\,^3P_1$-$2\,^3P_2$ interval. Such a correction, however, cannot explain the -1 kHz (4.9σ) discrepancy between the results from microwave measurement [22] and laser spectroscopy [6,19].

V. CONCLUSION

The light-force-induced frequency shift in the laser spectroscopy of an atomic beam was investigated experimentally and theoretically. Substantial modification of the trajectories of helium atoms in a standing-wave laser field was observed by a position-resolving detector, which had led to considerable distortions on the spectral lineshape. A master equation describing the dynamics of open quantum systems was presented, and the Monte Carlo wave-function approach was applied to simulate atomic trajectories with a quantum-mechanical treatment for the external motions. The simulated spectra reproduced not only the characteristics of the distortions in observed lineshape, but also the nonlinear dependence of the fitted line centers on the laser power. This effect was considerably large even with relatively low laser power for light atoms such as helium. Taking into account the light-force-induced shift at our experimental conditions, we assigned a correction of $+0.50(80)$ kHz to the $2\,^3S_1$-$2\,^3P_1$ transition frequency. Methods to suppress the light-force shift were also discussed, which will be applied in our new setup under construction to improve the accuracy of the atomic helium spectroscopy. A more accurate determination of the $2\,^3S$-$2\,^3P$ transition frequency of ^{4}He and ^{3}He may help to resolve the present disagreements in the ^{3}He-^{4}He nuclear charge radius difference derived from different transitions [9,23–25].

ACKNOWLEDGMENTS

This work is jointly supported by Natural Science Foundation of China (91736101, 21688102, 11304303,

91436209, 21427804), the Chinese Academy of Science (XDB21010400, XDB21020100), and the Ministry of Science and Technology of China (2013CB834602).

APPENDIX: MASTER EQUATION

In the quantized atomic center-of-mass (CM) motion description, the full Hamiltonian for the atom-laser system plus the vacuum field is

$$H = H_A + H_R + V_{A\text{-}L} + V_{A\text{-}R}, \tag{A1}$$

where $H_A = \hbar\omega_0 P_e + P^2/2m$ is the atomic Hamiltonian including both internal states and external motion, H_R is the vacuum radiation field Hamiltonian, and $V_{A\text{-}L}$ and $V_{A\text{-}R}$ are the atom-laser and atom-radiation field coupling terms, respectively. Note that, in the atomic Hamiltonian, $P_e = |e\rangle\langle e|$ is a projection operator onto the excited state, and P is the atomic CM momentum operator. The effects of atom-laser and atom-radiation-field coupling are assumed to be independent.

We can view Eq. (A1) in terms of "*system-reservoir*" interactions. The "small" *system* consists of the atom, laser, and their interaction. The *system* Hamiltonian H_S is

$$H_S = H_A + V_{A\text{-}L}. \tag{A2}$$

The *reservoir* in our case is the vacuum radiation field, which is supposed to be sufficiently large and into which energy is effectively and irreversibly dissipated.

With the Born–Markov approximation and other approximations, the master equation takes the Lindblad form

$$\frac{d(\rho_S)}{dt} = -\frac{i}{\hbar}[H_S, \rho_S] + \hat{\mathcal{L}}_{\text{relax}}[\rho_S], \tag{A3}$$

where ρ_S is the reduced density operator for the *system* in which the degrees of freedom of the *reservoir* have been traced over, $\rho_S = \text{Tr}_R[\rho]$. The remaining term, $\hat{\mathcal{L}}_{\text{relax}}[\rho]$, is the relaxation superoperator acting on the reduced density operator:

$$\hat{\mathcal{L}}_{\text{relax}}[\rho_S] = \sum_m \left[C_m \rho_S C_m^\dagger - \frac{1}{2}(C_m^\dagger C_m \rho_S + \rho_S C_m^\dagger C_m) \right], \tag{A4}$$

where C_m are the quantum jump operators acting in the space of the *small* system.

When taking the spontaneous emission including recoil into account, the relaxation superoperator can be written as [21,26]

$$\begin{aligned}\hat{\mathcal{L}}_{\text{relax}}(\rho_S) = &-(\Gamma/2)(P_e\rho_S + \rho_S P_e) \\ &+ (3\Gamma/8\pi)\int d^2\Omega \sum_{\epsilon\perp\mathbf{k}'} \exp(-i\mathbf{k}'\cdot\mathbf{R})(\epsilon^*\cdot S^-) \\ &\times \rho_S(\epsilon\cdot S^+)\exp(i\mathbf{k}'\cdot\mathbf{R}),\end{aligned} \tag{A5}$$

where $S^+ = |e\rangle\langle g|$ and $S^- = |g\rangle\langle e|$ are the rasing and lowering operators, respectively. The integral runs over the direction of the emitted photon, with a wave vector $\mathbf{k}'$ pointing in the direction of the solid angle Ω, and polarization ϵ are orthogonal to the wave vector.

The superoperator [Eq. (A4)] suggests to choose the jump operators as follows:

$$C_{\Omega,\epsilon} = \sqrt{\frac{3\Gamma}{8\pi}} e^{-i\mathbf{k}'\cdot\mathbf{R}}(\epsilon^*\cdot S^-). \tag{A6}$$

[1] F. Biraben, Eur. Phys. J. Spec. Top. **172**, 109 (2009).

[2] K. Pachucki and V. A. Yerokhin, Phys. Rev. Lett. **104**, 070403 (2010).

[3] C. G. Parthey, A. Matveev, J. Alnis, B. Bernhardt, A. Beyer, R. Holzwarth, A. Maistrou, R. Pohl, K. Predehl, T. Udem, T. Wilken, N. Kolachevsky, M. Abgrall, D. Rovera, C. Salomon, P. Laurent, and T. W. Hänsch, Phys. Rev. Lett. **107**, 203001 (2011).

[4] A. Matveev, C. G. Parthey, K. Predehl, J. Alnis, A. Beyer, R. Holzwarth, T. Udem, T. Wilken, N. Kolachevsky, M. Abgrall, D. Rovera, C. Salomon, P. Laurent, G. Grosche, O. Terra, T. Legero, H. Schnatz, S. Weyers, B. Altschul, and T. W. Hänsch, Phys. Rev. Lett. **110**, 230801 (2013).

[5] K. Pachucki, V. Patkóš, and V. A. Yerokhin, Phys. Rev. A **95**, 062510 (2017).

[6] X. Zheng, Y. R. Sun, J.-J. Chen, W. Jiang, K. Pachucki, and S.-M. Hu, Phys. Rev. Lett. **118**, 063001 (2017).

[7] V. Patkóš, V. A. Yerokhin, and K. Pachucki, Phys. Rev. A **94**, 052508 (2016).

[8] A. Beyer, L. Maisenbacher, A. Matveev, R. Pohl, K. Khabarova, A. Grinin, T. Lamour, D. C. Yost, T. W. Hänsch, N. Kolachevsky, and T. Udem, Science **358**, 79 (2017).

[9] X. Zheng, Y. R. Sun, J.-J. Chen, W. Jiang, K. Pachucki, and S.-M. Hu, Phys. Rev. Lett. **119**, 263002 (2017).

[10] P. C. Pastor, G. Giusfredi, P. De Natale, G. Hagel, C. de Mauro, and M. Inguscio, Phys. Rev. Lett. **92**, 023001 (2004); **97**, 139903 (2006).

[11] A. Beyer, L. Maisenbacher, A. Matveev, R. Pohl, K. Khabarova, Y. Chang, A. Grinin, T. Lamour, T. Shi, D. C. Yost, T. Udem, T. W. Hänsch, and N. Kolachevsky, Opt. Express **24**, 17470 (2016).

[12] M. G. Prentiss and S. Ezekiel, Phys. Rev. Lett. **56**, 46 (1986).

[13] C. E. Wieman, M. C. Noecker, B. P. Masterson, and J. Cooper, Phys. Rev. Lett. **58**, 1738 (1987).

[14] R. Grimm and J. Mlynek, Phys. Rev. Lett. **63**, 232 (1989).

[15] R. Grimm and J. Mlynek, Phys. Rev. A **42**, 2890 (1990).

[16] F. Minardi, M. Artoni, P. Cancio, M. Inguscio, G. Giusfredi, and I. Carusotto, Phys. Rev. A **60**, 4164 (1999).

[17] M. Artoni, I. Carusotto, and F. Minardi, Phys. Rev. A **62**, 023402 (2000).

[18] M. Smiciklas and D. Shiner, Phys. Rev. Lett. **105**, 123001 (2010).

[19] G.-P. Feng, X. Zheng, Y. R. Sun, and S.-M. Hu, Phys. Rev. A **91**, 030502 (2015).

[20] J. Dalibard, Y. Castin, and K. Mølmer, Phys. Rev. Lett. **68**, 580 (1992).

[21] K. Mølmer, Y. Castin, and J. Dalibard, J. Opt. Soc. Am. B **10**, 524 (1993).

[22] K. Kato, T. D. G. Skinner, and E. A. Hessels, Phys. Rev. Lett. **121**, 143002 (2018).

[23] D. Shiner, R. Dixson, and V. Vedantham, Phys. Rev. Lett. **74**, 3553 (1995).

[24] R. v. Rooij, J. S. Borbely, J. Simonet, M. D. Hoogerland, K. S. E. Eikema, R. A. Rozendaal, and W. Vassen, Science **333**, 196 (2011).

[25] P. Cancio Pastor, L. Consolino, G. Giusfredi, P. De Natale, M. Inguscio, V. A. Yerokhin, and K. Pachucki, Phys. Rev. Lett. **108**, 143001 (2012).

[26] J. Javanainen and S. Stenholrn, Appl. Phys. (Berlin) **21**, 35 (1980).